Numerical and Experimental Investigation of Primary Breakup of High-Viscous Fluid at Elevated Pressure

Feichi Zhang[1*], Thomas Müller[1], Thorsten Zirwes[2,1], Simon Wachter[3], Tobias Jakobs[3], Peter Habisreuther[1], Nikolaos Zarzalis[1], Dimosthenis Trimis[1], Thomas Kolb[3],

[1]Engler-Bunte-Institute/Combustion Technology, Karlsruhe Institute of Technology, Engler-Bunte-Ring 7, 76131, Karlsruhe, Germany
[2]Steinbuch Centre for Computing, Karlsruhe Institute of Technology, Hermann-von-Helmholtz-Platz 1, 76344 Eggenstein-Leopoldshafen
[3]Institut for Technical Chemistry, Karlsruhe Institute of Technology, Herrmann-von-Helmholtz-Platz 1, 76344 Eggenstein-Leopoldshafen
*Corresponding author: feichi.zhang@kit.edu

Abstract

Highly-resolved numerical simulations and high-speed camera measurements have been carried out for a generic test rig with an air-assisted, external mixing nozzle. Objective of the study is to access the effect of elevated pressure on the primary atomization of a high-viscous liquid jet. The viscosity of the liquid was varied by 1 and 100 mPas and the pressure from 1 to 6 bar. Different nozzle geometries were used to keep the gas-to-liquid ratio and exit velocity of the gas constant. The numerical and experimental results showed reasonably good agreement regarding morphological behaviors of the primary breakup process. A pulsating mode instability of the primary breakup followed by a fiber type disintegration of ligaments from the liquid core has been confirmed for all cases. An increased viscosity of the liquid phase leads to larger liquid ligaments and a smaller cone angle. At elevated pressure, finer liquid fragments are disintegrated and the liquid core contracts, causing a shorter breakup length and narrower liquid cone. The simulations reveal a strongly increased kinetic energy of the liquid at higher pressure, particularly in the high frequency range, which indicates a reinforced transfer of momentum from gas to liquid phase. For all considered cases, an exponential growth of the specific kinetic energy of liquid with decreasing volume fraction of liquid has been found, with an exponential decay rate close to unity. The enhanced momentum transfer is attributable to the increased Weber number with pressure or gas density, respectively. In addition, small-scale, high-frequency turbulent fluctuations is enhanced due to an increased Reynolds number at elevated pressure. The behavior of strengthened momentum transfer is in accordance with an increased gas-to-liquid momentum flux ratio, which should be considered as a relevant parameter for characterizing primary atomization.

Keywords

Twin-fluid Atomization; Primary Atomization; Elevated Pressure; Volume of Fluid - Large Eddy Simulation (VOF-LES); OpenFOAM;

Introduction

Entrained flow gasification (EFG) is widely used for the conversion of low-grade fossil or biogenic liquid fuels to syngas, which can further be utilized for the production of chemicals or power generation via combustion [1, 2, 3, 4]. Besides the complex gasification reactions, atomization of the liquid fuel plays a key role for the overall performance [5]. A well-distributed spray with small-scale droplets leads to a fast evaporation of liquid fuel, which improves performance of mixing and gasification of liquid vapor with oxygen gas. Gas-assisted nozzles are generally used for EFG, where a low-speed liquid stream is subjected to aerodynamic strain from the high-speed ambient gas flow and disintegrated by means of momentum transfer with the gas phase. The primary breakup of the liquid jet core determines the near-field behavior of the coaxial gas-liquid jets, and covers the initial deformation of liquid core till the generation of the first disintegrated liquid fragments. Therefore, the primary breakup phenomenon vitally connects the bulk liquid flow issuing from the atomizer and the final spray [6, 7, 8]. In the primary breakup process, the bulk flow of liquid is subjected to turbulent aerodynamic forces, which generate interfacial waves caused by Kelvin-Helmhotz instability; the most unstable waves become amplified according to Rayleigh-Taylor instability, leading to disintegration of thin liquid sheets from the intact jet core; the formed ligaments break down into droplets through the Rayleigh-Plateau instability [9]. Although this basic mechanism is well-known, a comprehensive knowledge for predicting the breakup characteristics is missing, as the breakup process is affected by a large number of system parameters, e.g. design parameters of the nozzle or material properties of liquid and gas. Also, the gas-liquid interaction through momentum transfer at their interface covers a wide range of length and time scale due to the highly turbulent nature of the gas flow [7]. Due to limited optical access and the lack of powerful diagnostics for detailed measurement of the multiphase flow field, previous experimental works on primary atomization mainly focused on the morphological behavior of the breakup process by shadowgraph images, and developing estimations for some basic properties as a function of the operating parameters, such as the breakup length or the cone angle [7, 10, 11, 12, 13, 14, 15, 16, 17, 18, 19, 20]. In these works, mostly water was atomized at atmospheric condition, whereas EFG is commonly operated with high-viscous liquids and at elevated pressure. As different

nozzles were applied in these works and the desired measurement values were not distinguishable for many test conditions due to experimental limitations, the available data and correlations are of questionable generality and the physics behind primary atomization is still not well understood. Additionally, it is not sufficient to describe atomization performance solely by scalar geometrical and operational parameters, but has to include the injection direction of the atomizing fluids in relation to each other and to the ambient (e.g., reactor chamber) [17, 21].

In an attempt to overcome these difficulties and to gain a more detailed insight into the breakup mechanism due to multiphase interaction, highly-resolved numerical simulations have been carried out in order to study primary atomization in a generic test rig, using an external-mixing air-assisted nozzle. The setup represents a simplified nozzle configuration of a real scale EFG device proposed in the framework of the Bioliq project [2, 22], which is specifically designed for fundamental investigations on the effect of selected operating parameters on the atomization at near-EFG conditions. Scope of this work is to study the influence of elevated pressure on the primary breakup process at constant gas-to-liquid mass and momentum ratio. For that purpose, numerical simulations have been performed for two liquids with different dynamic viscosities (water and glycerin-water mixture) and the system pressure has been varied from 1 to 6 bar. The numerical results are validated by means of high-speed camera measurement.

Experimental and Numerical Setups
Pressurized Atomization Test Rig - PAT

The atomization test rig includes an air-assisted nozzle with a central cylindrical liquid stream surrounded by an annular air flow, which is capable of being operated at elevated pressure conditions. A detailed description of the test rig can be found in [19, 20]. For the current study, water and glycerol/water mixture (mass fraction of glycerol = 84.3%) have been used as model fluids. The temperature was kept constant at T_0 = 293 K. The mass flow rate of liquid is $\dot{m}_L$ = 20 kg/h and that of the annular airflow is $\dot{m}_G$ = 16 kg/h, leading to a gas liquid ratio of GLR = 0.8. The diameter of the orifice of the round liquid jet at nozzle exit is d_L = 2 mm and the width of the web separating the central liquid from the co-flow air is s = 0.1 mm. In order to keep the momentum ratio and relative velocity constant at given GLR, the outlet area of the annular duct for the air stream is adjusted to be decreasing proportionally with increasing system pressure, as shown in Fig.1. In this way, the mass flow rate, the bulk velocity of the airflow and the relative velocity between liquid and gas streams remain constant at different pressures.
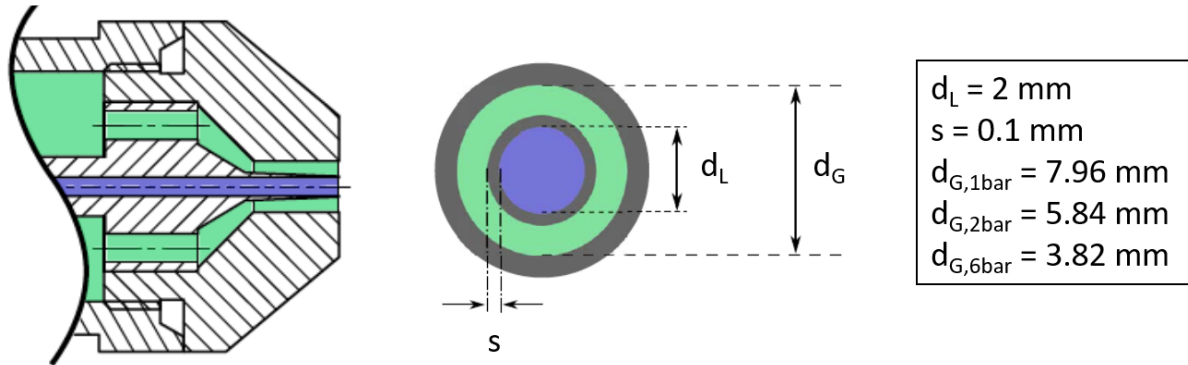

d_L = 2 mm
s = 0.1 mm
$d_{G,1bar}$ = 7.96 mm
$d_{G,2bar}$ = 5.84 mm
$d_{G,6bar}$ = 3.82 mm

Figure 1. Sketch of the used twin-fluid atomizer.

Tab.1 lists basic physical properties of the considered fluids, where μ, ρ and σ denote the dynamic viscosity, the density and the surface tension. The Ohnesorge number and the Reynolds number of liquid flow are calculated by

$$Oh = \frac{\mu_L}{\sqrt{\rho_L d_L \sigma}}, \quad Re_L = \frac{\rho_L u_L d_L}{\mu_L}, \quad u_L = \dot{m}_L/\rho_L/A_L, \quad A_L = \frac{1}{4}\pi d_L^2 \tag{1}$$

with the bulk flow velocity of the liquid jet u_L and the cross-sectional area of liquid stream A_L. k_L denotes the specific kinetic energy per unit liquid volume calculated with $k_L = \frac{1}{2}\rho_L u_L^2$. It is noteworthy that Re_L is decreased and Oh increased by a factor of approx. 100 by using the glycerol/water mixture instead of water. Tab.2 provides important dimensionless parameters for the gaseous flow, which assists the atomization: the gas-to-liquid momentum ratio, the gas-to-liquid momentum flux ratio M, the aerodynamic Weber number We and the gasous Reynolds number Re_G

$$MR = \frac{\rho_G u_G^2 A_G}{\rho_L u_L^2 A_L}, \quad M = \frac{\rho_G u_G^2}{\rho_L u_L^2}, \quad We = \frac{\rho_G u_{rel}^2 d_L}{\sigma}, \quad Re_G = \frac{\rho_G u_G d_G}{\mu_G} \tag{2}$$

where $u_G = \dot{m}_G/\rho_G/A_G$ is the gaseous bulk velocity, A_G the annular outlet area of air stream and $u_{rel} = u_G - u_L$ the relative velocity between the gas and liquid flow. As u_G remains constant with increasing p_0, M, We and Re_G correlate linearly with p_0 or gas density ρ_G, respectively. The momentum ratio MR remains constant while varying the pressure. A high speed camera has been used to diagnose the primary breakup process near the nozzle exit, using a frame rate of 12 kHz and a spatial resolution of 62.5 μm per pixel for a region of 640×480 pixel.

**Table 1.** Material properties of model liquids and air at $T_0 = 293$ K $p_0 = 1$ bar.

Fluid	μ [mPa·s]	ρ [kg/m^3]	σ [N/m]	Oh [-]	Re_L [-]	k_L [J/m$_L^3$]
Water	1	998	72.8	0.0026	3537	1563
Glycerol/water	100	1223	64.8	0.2522	35.4	1279
Air	0.0182	1.205	–	–	–	

Table 2. Dimensionless paramters at different operating pressures.

Gas		Water			Glycerol/water mixture		
p_0 [bar]	Re_G [-]	MR [-]	M [-]	We [-]	MR [-]	M [-]	We [-]
1	30,600	36.6	2.5	207	43.9	3	234
2	38,600	36.6	5	414	43.9	6	469
6	51,600	36.6	15	1244	43.9	18	1409

Numerical Setups

The computational domain was deliberately designed to include a major part of the nozzle system, which allows the development of turbulent flows within the nozzle. As depicted in Fig.2 in the subplot on the left, it includes a central tube of 50 mm length for the liquid flow and annularly arranged tubes for the air flow with 25 mm extension into the nozzle. A spreading cone region with the size of 60 mm in length and 20 mm to 40 mm in diameter was used for the atomization region. The computational grids for different pressures consist of approx. 7.3 million tetrahedral finite volumes with low aspect ratio. Fig.2 shows a meridian cut-plane of the computational grid passing through the centerline axis (top left) and the overall surface mesh (middle), along with indications of boundary conditions. The near-nozzle zone is locally refined with an equidistant resolution of $\Delta = 80\ \mu\text{m}$ for all spatial directions.
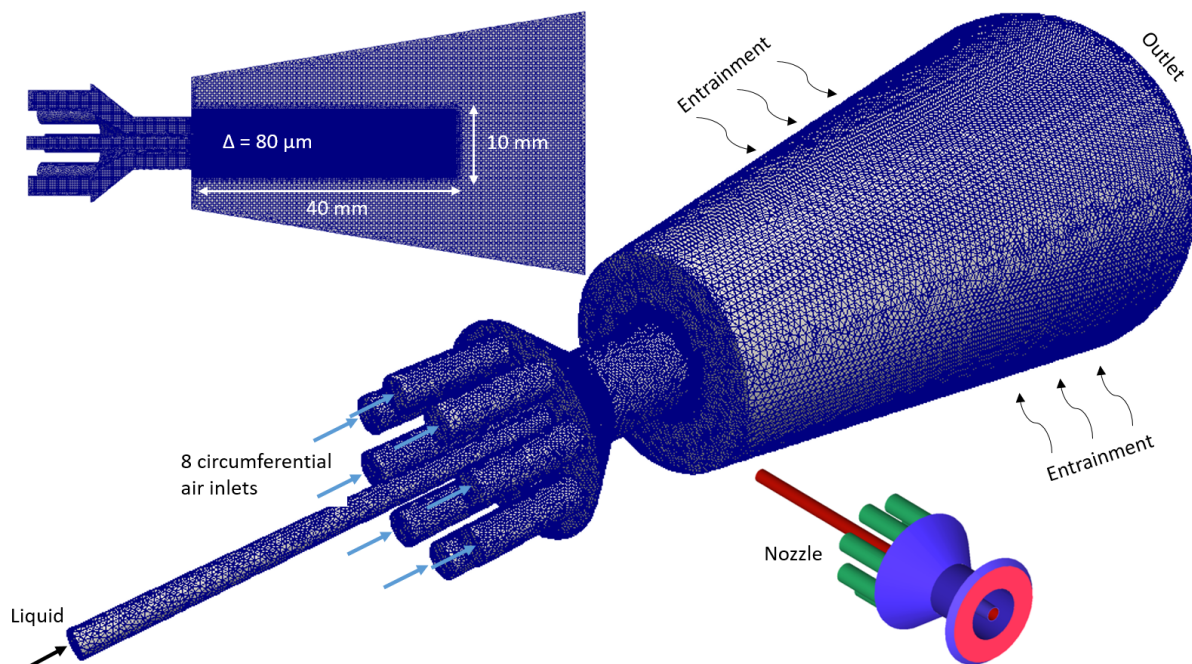
Figure 2. Cutting plane of the computational grid passing through the centerline axis (top left), surface mesh of overall grid (middle) and isometric view of the nozzle (bottom right).

The multiphase flow simulations have been conducted with the standard solver "compressibleInterFoam" from the open-source CFD code library OpenFOAM [23]. It applies the volume of fluid method (VOF) for capturing the gas-liquid interface, solving a transport equation for the volume fraction of liquid phase in addition to the continuity and momentum equations. A detailed description of the implementation of the VOF method in OpenFOAM can be found in [24, 25]. Both, gaseous and liquid phase, were considered as Newtonian fluids. The turbulent flow field is modeled by means of the large eddy simulation (LES) technique with the wall-adapted local eddy viscosity (WALE) sub-grid scale model [26]. The equation set has been solved in their compressible formulation, employing the finite

volume method [27]. An implicit scheme of 2nd order accuracy (CrankNicolson) has been used for time integration; the convection and diffusion terms were discretized with 2nd order schemes, too. The time step was selected appropriately low to allow the maximum CFL number being below 0.4. After a statistically converged solution was achieved, 1 million time steps, corresponding to a physical time of 0.05 s, have been used for averaging the flow field in the near-nozzle zone.

As the resolution is not sufficient to resolve the whole range of droplet sizes during atomization, the focus of the present work is laid on resolving primary breakup of the intact liquid core as well as the disintegration of large-scale liquid ligaments from the core jet. Apart from the liquid core, liquid fragments are essentially resolved till the cut-off scale by the VOF method. Large scale liquid ligaments can be properly resolved and droplets smaller than the grid length are smeared out over the computational cells, leading to values of liquid volume fractions smaller than unity. In this way, the VOF method is suited to reproduce the primary breakup behavior of liquid jet, along with the dispersions of disintegrated liquid elements due to the turbulent flow. Therefore, a comparison between line-of-sight measurement and VOF simulation is feasible for the range of dense liquid region, for example, for an assessment of the cone angle of the jet or the penetration range of liquid fragments, but not for the droplet size distributions.

Results and Discussion
Morphological Characteristics

In Fig.3, high-speed camera images are shown together with calculated instantaneous and time-mean contours of the liquid volume fraction f and $\bar{f}$ for a cutting plane passing through the centerline axis: at the top for $\mu = 1$ mPas, at the bottom for $\mu = 100$ mPas, on the left for $p = 2$ bar and on the right for $p = 6$ bar. The white solid curves in $\bar{f}$ indicate iso-values of $\bar{f} = 0.1$, 0.5 and 0.9, which help in indentifying the length and the spreading of the liquid jet core. As small-scale liquid fragments or droplets cannot be resolved with the present grid resolution, their volumes are smeared over the computational cells, leading to continuously distributed small values of f in dense liquid zones. f and $\bar{f}$ are therefore displayed in logarithmic scale in order to visualize the entire region of liquid volume. In agreement with the high-speed camera measurement, the VOF-LES simulations reveal a fiber-type breakup of the liquid jet for all cases, which is dominated by a pulsating mode instability. The intact liquid core is therewith deflected slightly from the center axis and small-scale liquid fragments disintegrate from the liquid core.
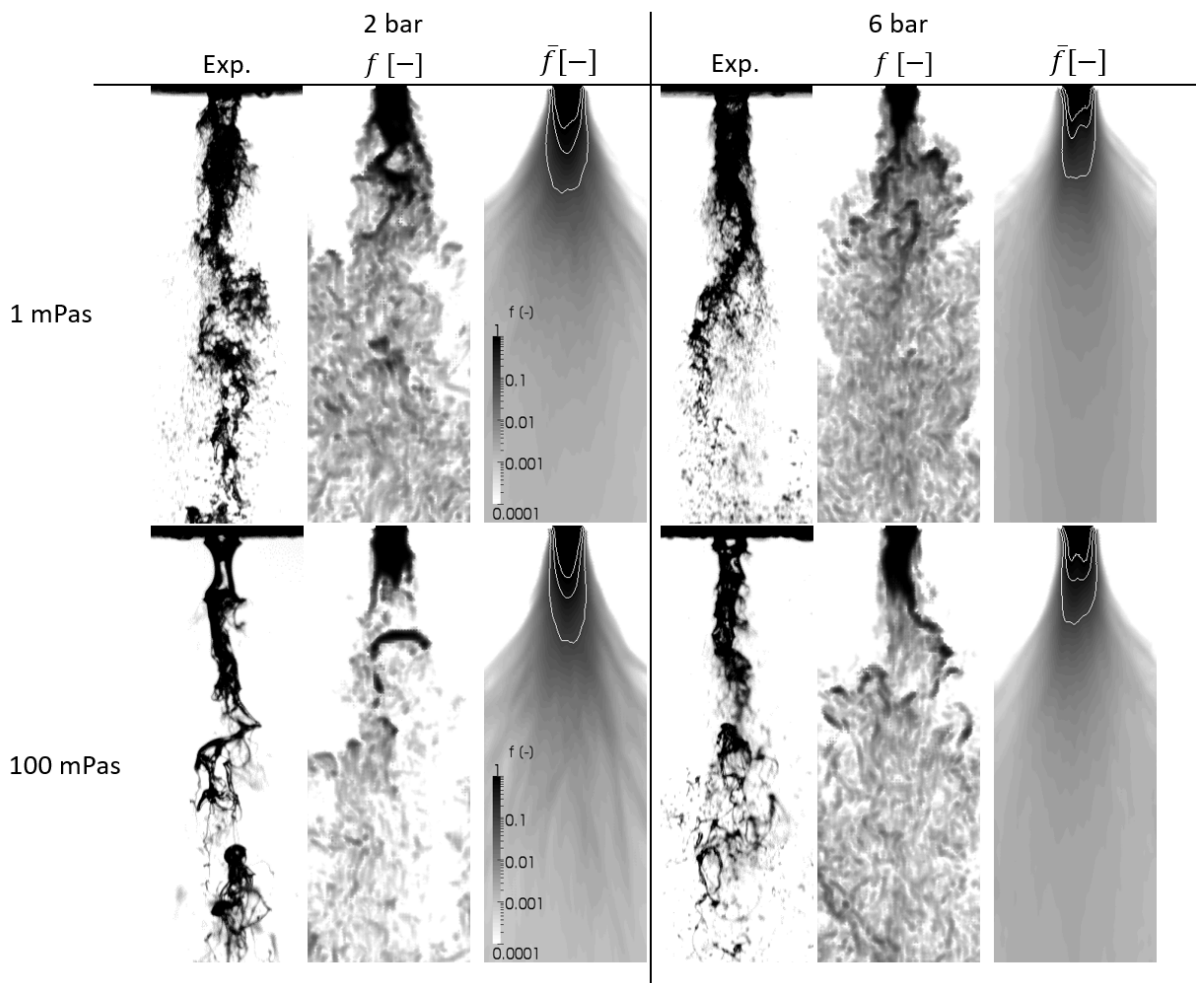

Figure 3. Comparison of high-speed camera images with calculated volume fractions of liquid by VOF-LES for different liquid viscosities (top and bottom for 1 and 100 mPas) and ambient pressures (left and right for 2 and 6 bar).

Despite the viscosity of liquid being increased by a factor of 100 by using glycerol/water mixture instead of water, this change has only minor impact on the measured and simulated morphological behavior of the breakup process for the operating conditions under investigation. The liquid core length increases and the spreading of spray decreases slightly in this case, which can be identified by comparing contours of $\bar{f}$ between the upper and lower plots in Fig.3. As an increased liquid viscosity lowers the Reynolds number (see Tab.1) and hinders the growth of intrinsic instabilities through generation of liquid sheets, larger liquid ligaments are formed due to a delayed onset of jet disintegration [5].

A higher system pressure results in a higher We and Re in the gas phase due to an increased gas density and a decreased kinematic viscosity. Consequently, turbulent fluctuations in the gas phase and aerodynamic forces acting on the liquid phase are reinforced at elevated pressure, which promote aerodynamic instabilities at the liquid-gas interface. The liquid core contracts in this case, leading to a slightly decreased length the core jet with increased pressure, as shown in Fig.3 by the iso-$\bar{f}$ contours. These results correspond to previous experimental and numerical investigations by Müller et al. [28], where the ambient pressure was varied without changing the geometry of the nozzle. The decrease of breakup length with increased We and M was also reported in [11, 13]. In addition, as small-scale turbulence fluctuations become more prominent with increased pressures or gaseous Re, finer ligaments disintegrate from the intact core at high pressures, as illustrated by the high-speed camera picture. Although not shown here, similar results regarding morphological phenomena have been found for the atmospheric pressure case with both water and glycerol/water mixture.

Fig.4 shows profiles of the time-mean (left) and time-rms (root mean square, right) values of f along the centerline axis. For both low and high viscous liquids, an increased pressure leads to an ealier decay of $\bar{f}$ in downstream direction, confirming again the decrease of liquid core length with pressure. The same behavior can also be detected by the profile of f', where its maximum value f'_{max} moves upstream. f'_{max} reveals in this case the most intense fluctuation of liquid volume fraction, which corresponds to the location with the largest gradient of $\bar{f}$ and is expected to occur at the breakup length, where liquid ligaments start to detach from the liquid jet. f'_{max} decreases with increasing pressure, which points out damped fluctuations of f or reduced length scales of disintegrated liquid fragments, respectively.
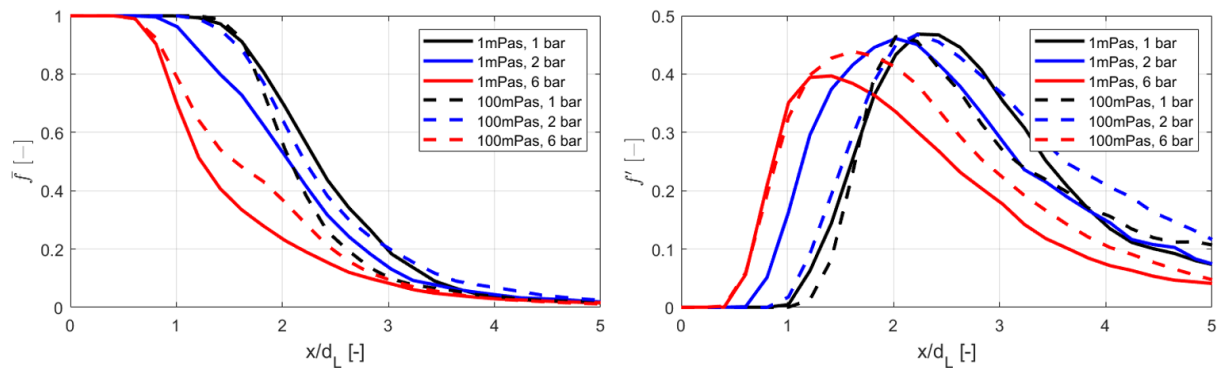

Figure 4. Distributions of time-mean (left) and time-rms (right) values of liquid volume fraction along the centerline axis.

Momentum Transfer from Gas to Liquid

In oder to assess the change of liquid's kinetic energy due to momentum transfer from the gas to liquid phase, the liquid's kinetic energy per cell volume and per liquid volume, $k_L^0 = \frac{1}{2}f\rho_L\vec{v}^{\,2}$ and $k_L^1 = \frac{1}{2}\rho_L\vec{v}^{\,2}$ with the flow velocity $\vec{v}$, have been considered as suitable parameters. As the initial mass flow and momentum of the liquid stream are constant while varying the pressures, an increase in k_L^0 or k_L^1 denotes specifically an enhanced transfer of momentum between different phases.

In Fig.5, contours of k_L^0 are shown for the $f = 0.01$ iso-surface and a meridian cut-plane. k_L^0 increases locally and the regions of large k_L^0 value extend further downstream with elevated pressure, although the length of the core jet decreases with pressure (see Fig.3 and Fig.4). The same trend can be noticed in the left subplot of Fig.6. There, the time-averaged k_L^0 normalized to the initial specific kinetic energy of liquid k_L (see Tab.1) is higher in case of elevated pressure, even in regions where the volume fraction of liquid is much smaller (see Fig.4 on the left). Therefore, despite k_L^0 being calculated by means of $k_L^0 \propto f\rho_L\vec{v}^{\,2}$, it decreases with f. This is due to the specific kinetic energy per unit liquid volume $k_L^1 = k_L^0/f$ increasing in a rate, that is much larger than the decay rate of f, as shown in Fig.6 on the right. Comparing the streamwise distributions of $\bar{f}$ in Fig.4 on the left and $\bar{k}_L^1/k_L$ in Fig.6 on the right, a rapid increase of k_L^1 starting from the locations of breakup length is observed, whereas the rate of decreasing $\bar{f}$ is relatively small. This points out a drastically enhanced momentum transfer from the turbulent gas flow to liquid fragments, as soon as these are disintegrated from the liquid core. Both water and glycerol/water mixture show a monotonous rise of $\bar{k}_L^1$ with pressure and $\bar{k}_L^1$ is higher for the glycerol/water mixture at constant pressure, which correlates with the increased We or M (see Tab.2). The effect of μ_L or Oh on the momentum transfer may be subordinate compared to that of We or M, as an increase in μ_L or Oh by a factor of 100 only leads to a relatively small variation of $\bar{k}_L^1$.
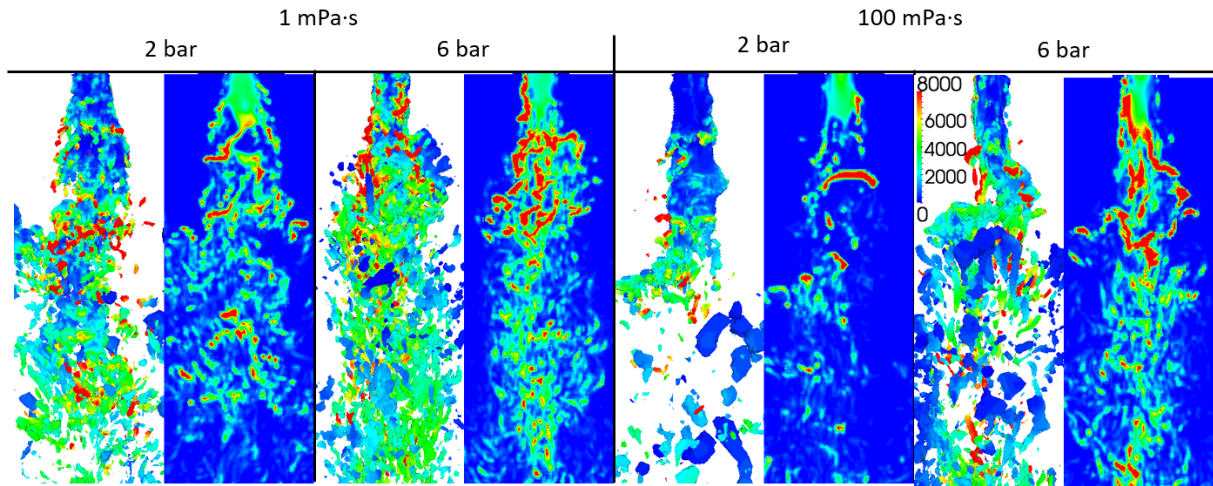
Figure 5. 3D iso-surfaces of f = 0.01 colored by liquid's kinetic energy and contours of liquid's kinetic energy on a cutting plane passing through the centerline axis for different liquid viscosities (1 and 100 mPas) and ambient pressures (2 and 6 bar).
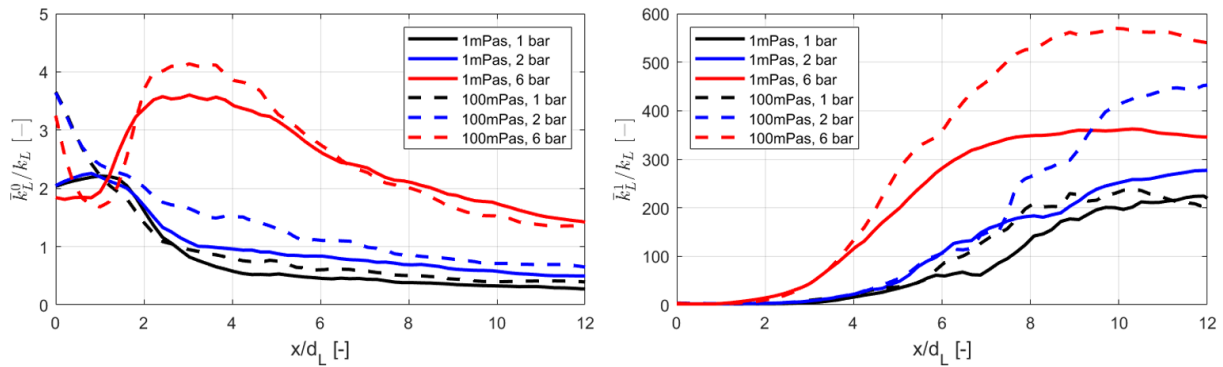

Figure 6. Streamwise distributions of time-mean liquid's kinetic energy per total volume (left) and per liquid volume (right).

The same behavior can be detected in Fig.7, where $\bar{k}_L^1$ and $\bar{f}$ collected from the centerline axis are plotted against each other, on the left in linear scale and on the right in double logarithmic scale. $\bar{k}_L^1$ decreases with $\bar{f}$ in almost an exponential way. In this case, as the volume fraction of liquid decreases due to collapse of the liquid core jet, the momentum transfer from ambient turbulent gas to the liquid phase increases significantly. The effect is particularly large in the range with $\bar{f} < 0.05$, where a rapid rise of $\bar{k}_L^1$ with decreasing $\bar{f}$ is apparent. The double-logarithmic plots of $\bar{k}_L^1(\bar{f})$ shown on the right of Fig.7 yield almost a linear progress for all cases, leading to a power law correlation of $\bar{k}_L^1 = a \cdot e^{-b\bar{f}}$ with an almost constant decay rate b close to unity, and an increasing pre-exponential coefficent a with pressure or We and M, respectively.
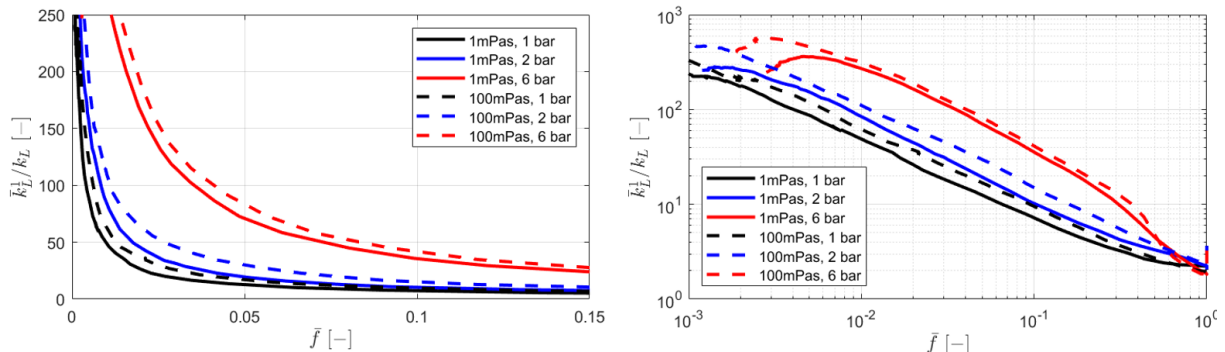

Figure 7. Time-mean specific kinetic energy of liquid plotted against the time-mean liquid volume fraction: on the left in normal scale and on the right in double logarithmic scale.

Spectral Behavior

Fig.8 shows spectral density of liquid kinetic energy $E_{k_L^0}$ for 3 monitor points located along the centerline axis downstream of the nozzle: $x/d_L = 2$, 4 and 8. $E_{k_L^0}$ is calculated from fourier transformation of sampled k_L^0 signals at different locations, which is a measure of the temporal fluctuation of k_L^0 as a function of oscillating frequency. $E_{k_L^0}$ increases in downstream direction from $x/d_L = 2$ to $x/d_L = 4$, especially in the high frequency range. In this case, small-scale liquid fragments are disintegrated from intact liquid jet core, which leads to a higher gas-to-liquid momentum ratio or enhanced aerodynamic interference on the liquid phase, respectively. $E_{k_L^0}$ decreases again from $x/d_L = 4$ to $x/d_L = 8$ due to a considerably lowered liquid volume fraction (see Fig.4 on the left) and the dissipation of gaseous turbulent kinetic energy (see Fig.6 on the left). $E_{k_L^0}$ is generally higher while increasing the operation pressure, which indicates an intensified multiphase interaction in terms of momentum exchange at elevated pressure. The effect is particularly perceptible in the high frequency range (see $x/d_L = 2$ in Fig.8) due to an increased turbulent kinetic energy of small-scale vortices through an increased gaseous Re or decreased gaseous kinematic viscosity. As a consequence, the increase of k_L^0 with pressure is mainly attributable to the enhanced high-frequency momentum exchange between gas and liquid phases at even smaller length scales. This behavior can also be detected from Fig.7 on the left, where k_L^0 increases faster at elevated pressure with decreasing volume fraction of liquid.
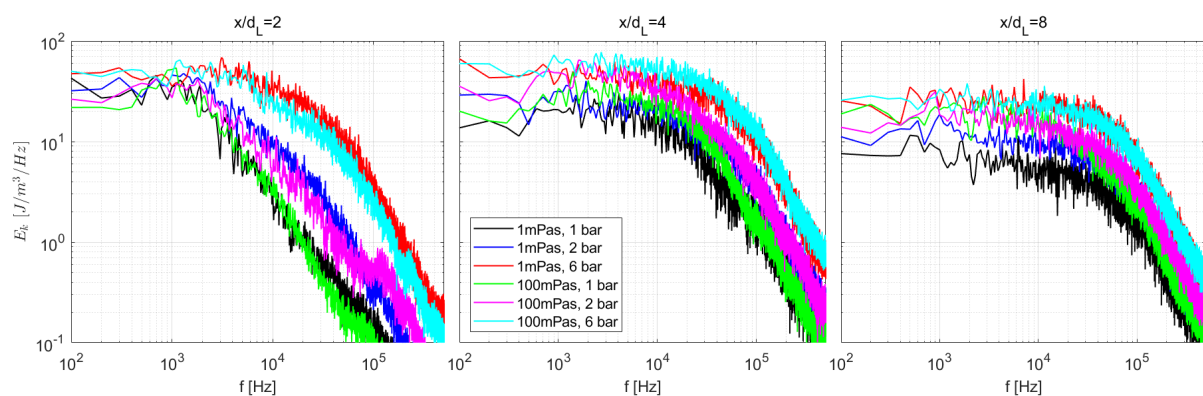

Figure 8. Spectra of calculated liquid's kinetic energy for 3 different locations along the centerline axis.

Conclusions

Highly resolved numerical simulations and high-speed camera measurements have been conducted for a generic test rig for studying the effect of elevated ambient pressures on the primary atomization of high-viscous liquid, while keeping the mass flows and gas-to-liquid ratio constant. Both numerical and experimental results showed a reasonable agreement regarding important breakup characteristics such as breakup regime, breakup length and dispersion. Increasing the viscosity of the liquid or Oh by a factor 100 leads to a narrower cone angle and larger liquid fragments disintegrated from the liquid jet core; the breakup length increases slightly for the higher viscous liquid. An increase in gas pressure results in a discernible shorter breakup length. The cone angle of liquid jet of liquid cone decreases and smaller liquid fragments are generated at higher pressure.

The momentum transfer from gas to liquid was found to be strongly reinforced after the location of breakup length and with increased ambient pressure, resulting in an increase of the kinetic energy of the liquid. This is attributted to the increased density or gas-to-liquid momentum flux ratio, causing an enhanced aerodynamic force acting on the gas-liquid interface. The effect was particularly significant for small-scale liquid fragments with low volume fractions due to the higher Re of the gas flow at elevated pressure. Consequently, turbulence energy is shifted towards high wave numbers, so that small-scale turbulent fluctuations, as well as their interaction with liquid phase, are reinforced at elevated pressure. For different cases with varied gas pressures and liquid viscosities, the strenghened momentum transfer was confirmed to be in accordance with an increased gas-to-liquid momentum ratio, which may be considered as a suitable parameter for characterizing momentum transfer during primary atomization. The specific kinetic energy of liquid showed a quasi-linear correlation with liquid volume fraction in double-logarithmic scale, with an almost constant decay rate close to unity. The correlation may be used to estimate liquid kinetic energy due to momentum transfer from gas to liquid phase for studying primary atomization.

Future work includes more detailed analysis of the correlation of momentum exchange behavior based on the momentum flux ratio, as well as simulations of the present setup with finer grid resolutions, in order to further justify validity of the obtained results.

Acknowledgements

Nomenclature

$a,\ b$	fitting coefficients of power function [-]
$A_L,\ A_G$	surface areas at nozzle exit for liquid, gas flow [m^2]
$d_L,\ d_G$	outer diameters of liquid, gas tubes [m]
f	frequency [Hz]
f	volume fraction of liquid [-]
k_L	specific kinetic energy of liquid within the nozzle [J/m$_L^3$]
k_L^0	specific kinetic energy of liquid per unit volume [J/m^3]
k_L^1	specific kinetic energy of liquid per unit liquid volume [J/m$_L^3$]
p_0	ambient pressure [Pa]
T_0	ambient temperature [K]
u_L, u_G	flow velocity of liquid, gas flow at nozzle exit [m/s]
v	resolved flow velocity from VOF-LES [m/s]
μ_L, μ_G	dynamic viscosity of liquid, gas flow [Pa·s]
ρ_L, ρ_G	density of liquid, gas [kg/m^3]
σ	surface tension [N/m]
MR	gas-to-liquid momentum ratio [-]
M	gas-to-liquid momentum flux ratio [-]
Oh	Ohnesorge number [-]
Re	Reynolds number [-]
We	Weber number [-]
$\bar{\cdot},\ \cdot'$	Time mean, rms values [-]

References

[1] Higman, C., Burgt, M., 2008, "Gasification". 2nd edition, Gulf Professional Publishing.
[2] Kolb, T., Aigner, M., Kneer, R., Müller, M., Weber, R., Djordjevic, N., 2016, *Journal of the Energy Institute*, 89 (4), pp. 485-503.
[3] Svoboda, K., Pohorely, M., Hartman, M., Martinec, J., 2009, *Fuel Processing Technology*, 90, pp. 629-635.
[4] Zhao, H., Liu, H., Xu, J., Li, W., Cheng, W., 2012, *Chemical Engineering Science*, 78, pp. 63-74.
[5] Levebvre, A.H., and. Mcdonell, V.G., 2017, "Atomization and Sprays". 2nd edition. Taylor & Francis Group, LLC.
[6] Chigier, N., Sept. 5.–7. 2005, Proceedings of ILASS-Europe 2005.
[7] Dumouchel, C., 2008, *Experiments in Fluids*, 45(3), pp. 371-422.
[8] Tian, X., Zhao, H., Liu, H., Li, W., Xu, J., 2014, *Chemical Engineering Science*, 107, pp. 93-101.
[9] Marmottant, P., and Villermaux, E., 2004, *Physics of Fluids A Fluid Dynamics*, 498, pp. 73-111.
[10] Farago, Z., and Chigier, N., Jun. 11. 1990, ASME 1990 International Gas Turbine and Aeroengine Congress and Exposition.
[11] Farago, Z., and Chigier, N., 1992, *Atomization and Sprays*, 2(2), pp. 137-153.
[12] Woodward, RD., Burch, RL., Kuo, KK., Cheung, FB., Jul. 18.–22. 1994, Proceedings of ICLASS'94.
[13] Engelbert, C., Hardalupus, Y., and Whitelaw, J., 1995, *Proc. R. Soc.*, 451, pp. 189–229.
[14] Lasheras, J. C., Villermaux, E., and Hopfinger, E. J., 1998, *Journal of Fluid Mechanics*, 357, pp. 351-379.
[15] Lasheras, J. C., and Hopfinger, E. J., 2000, *Annual Review of Fluid Mechanics*, 32(1), pp. 275-308.
[16] Shavit, U., 2001, *Experiments in Fluids*, 31, pp. 550-557.
[17] Mayer, W. O. H, Branam, R., 2004, *Experiments in Fluids*, 36, pp. 528-539.
[18] Jakobs, T., Djordjevic, N., Fleck, S., Mancini, M., Weber, R., Kolb, T., 2012, *Applied Energy*, 93, pp. 449-456.
[19] Sänger, A., Jakobs, T., Djordjevic, N., and Kolb, T., 2015, Proceedings 13th International Conference on Liquid Atomization & Spray Systems.
[20] Jakobs, T., Djordjevic, N., Sanger, A., Zarzalis, N., and Kolb, T., 2015, *Atomization and Sprays*, 25(12), pp. 1081-1105.
[21] Müller, T., Dullenkopf, A., Habisreuther, P., Zarzalis, N., Sänger, A., Jakobs, T., and Kolb, T., June 26.- 30. 2017, ASME Turbomachinery Technical Conference and Exposition, GT2017-63198.
[22] bioliq, https://www.bioliq.de/english/
[23] OpenFOAM. The Open Source CFD Toolbox, https://www.openfoam.com/releases/openfoam-v1806/
[24] Damin, S. M., 2012, "Description and utilization of interfoam multiphase solver". International Center for Computational Methods in Engineering.
[25] Müller, T., Sänger, A., Habisreuther, P., Jakobs, T., Trimis, D., Kolb, T., and Zarzalis, N., 2016, *International Journal of Multiphase Flow*, 87, pp. 212-228.
[26] Fröhlich, J., 2006, "Large Eddy Simulation turbulenter Strömungen". Teubner Verlag.
[27] Ferziger, J. H., and Peric M., 2002, "Computational Methods for Fluid Dynamics". Springer.
[28] Müller, T., Kadel, K., Habisreuther, P., Trimis, D., Zarzalis, N., Sänger, A., Jakobs, T., Kolb, T., Jun. 11.-15. 2018, ASME Turbomachinery Technical Conference and Exposition, GT2018-75950.